Soft x-ray angle-resolved photoemission spectroscopy on Ag(001): Band mapping, photon momentum effects, and circular dichroism

F. Venturini,[1] J. Minár,[2] J. Braun,[2] H. Ebert,[2] and N. B. Brookes[1]
[1]*European Synchrotron Radiation Facility (ESRF), Boîte Postale 220, 38043 Grenoble, France*
[2]*Department Chemie und Biochemie, Physikalische Chemie, Universität München, Butenandtstrasse 5-13, D-81377 München, Germany*

(Received 25 July 2007; revised manuscript received 13 November 2007; published 23 January 2008)

The (001) surface of silver (Ag) has been chosen as a simple and well known system for investigating the band mapping potential of angle-resolved photoemission spectroscopy in the soft x-ray energy range. Low temperature data of the valence band of Ag have been measured for four different high symmetry directions in reciprocal space. Furthermore, in order to determine the intrinsic limits of this technique, the issue of phonon-assisted nondirect transitions is addressed, both as a function of the measuring temperature and the incoming photon energy. The experimental data are directly compared with fully relativistic one-step model photoemission calculations. In particular, photon momentum transfer effects, which are often neglected in this energy regime, are discussed in detail. Finally, the experimental observation of circular dichroism in the angular distribution of the emitted photoelectrons allows for a comparison with the first calculated angle-resolved photoemission spectra showing this effect.

DOI: 10.1103/PhysRevB.77.045126 PACS number(s): 79.60.−i, 74.25.Jb, 74.25.Kc, 71.15.−m

I. INTRODUCTION

Angle-resolved photoemission spectroscopy (ARPES)[1,2] is well known for being a powerful and direct tool for probing the occupied electronic states of solids and, recently, great improvements have been made in both the energy and the angular resolution that can be obtained with the technique.[3,4] Such an advancement, however, has not been extended to three-dimensional systems, the major limitation being that, due to the lack of translational symmetry along the surface normal, the electron momentum in this direction is not conserved. The assumption of a free-electron-like final state has, historically, allowed us to determine a considerable number of three-dimensional band structures by measuring normal emission spectra as a function of the excitation energy. Nevertheless, such an approximation must be considered with care, as it is questionable for low excitation energies, especially so in the case of strongly correlated systems. For these, the availability of photons belonging to the soft x-ray energy range ($400\ \text{eV} \leqslant h\nu \leqslant 1500\ \text{eV}$) guarantees, upon excitation, the formation of a photoelectron final state that is effectively decoupled from the remaining system. Added to this, if the photon energy is increased to the soft x-ray range, the angle needed to cover a Brillouin zone (BZ) becomes considerably smaller if compared to the low energy application of the same technique. As a consequence, the corresponding **k**-space curvature is negligible when compared to the BZ size and the energy dispersion along any high symmetry direction can be measured directly. Also, for systems whose electronic structure differs markedly from surface to bulk,[5] higher incoming energies ensure more bulk representative results,[6–8] due to the increase of the inelastic mean free path. However, several issues hamper an unconditional use of this technique in the soft x-ray range. First of all, the measurements can suffer from momentum averaging effects, brought by the participation of the phonons in the photoemission process, that prevent accurate band mapping experiments. A different but equally important issue is the role of the photon momentum, $q = 2\pi/\lambda$, that can no longer be neglected as is justifiably done in the low photon energy regime. To give an example, in the particular case of silver (Ag), whose lattice constant and radius of the BZ are, respectively, $a = 4.09\ \text{Å}^{-1}$ and $2\pi/a = 1.54\ \text{Å}^{-1}$, at $h\nu = 21.2$ eV the photon momentum is only 0.5% of the BZ radius whereas for $h\nu = 1487$ eV it is nearly 50%. However, as will be shown in the following, despite the relatively high incoming energies, a careful choice of the experimental geometry can minimize the effect of q. From a more technical point of view, due to the strong decrease of the photoionization cross section with increasing photon energy,[9] high energy resolution measurements are very demanding and the development of the technique has represented a major challenge. Last but not the least, high angular resolution is also required since the momentum resolution not only depends on the angular resolution but also on the square root of the kinetic energy. Nowadays, thanks to the availability of dedicated photoemission beamlines that ensure a high photon flux at the sample, a high energy resolution of the monochromatized light, and a high performance of the electron analyzer, measuring soft x-ray angle-resolved photoemission spectra with relatively high energy and momentum resolution is possible.[6–8,10–15]

In this paper we discuss the potential of soft x-ray angle-resolved photoemission spectroscopy. In order to investigate the possibility of performing accurate band mapping experiments in the soft x-ray energy range, Ag has been chosen as a well known metal whose electronic band structure has been extensively studied both from a theoretical[16–22] and an experimental point of view.[23–31] Angle-resolved measurements of the valence band of the (001) surface of Ag are presented for four different high symmetry directions in reciprocal space and the good agreement with band structure calculations is discussed.[22] Given the no longer negligible role of the photon momentum, particular attention is devoted to the influence of its component parallel to the surface, q_{par}, on a

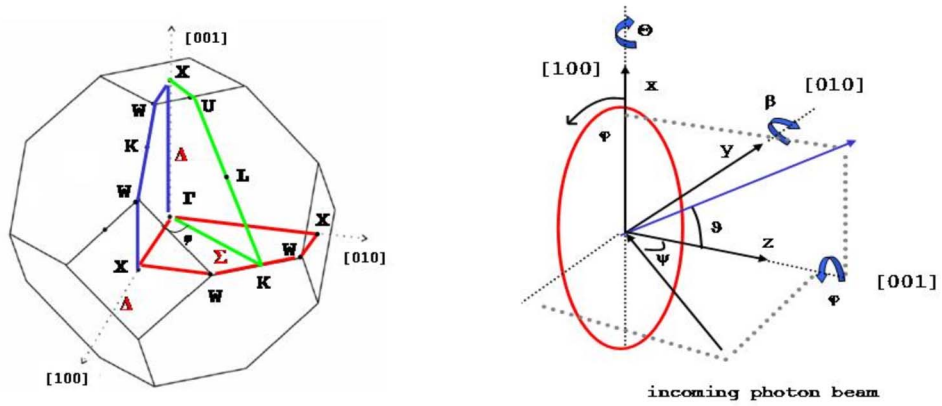

FIG. 1. (Color online) Left: BZ of Ag with high symmetry points and directions labeled with capital Roman and Greek letters, respectively. The blue and green lines show the two investigated emission planes, for $\varphi=0°$ and $\varphi=45°$, respectively. The (001) surface is highlighted in red. Right: schematic representation of the experimental geometry. The angle of incidence of the light with respect to the [001] direction is fixed and $\psi=35°$. The photoelectron emission plane is normal to the plane containing the incident light and the normal to the surface. Different emission planes can be probed by varying the azimuthal angle, φ.

precise band mapping procedure. It is shown that q_{par} does indeed modify the position in **k** space from where the direct transitions occur but, also, that this effect can be minimized by choosing the experimental geometry with care. Furthermore, in order to determine the intrinsic limits of the technique, the issue of phonon-assisted nondirect transitions is also addressed. To do so, measurements along one high symmetry direction have been recorded for different values of both the incoming photon energy and the temperature. The possibility of performing accurate band mapping experiments within the soft x-ray range is clearly evidenced, although the Debye temperature of the investigated system plays an important role in determining the appropriate temperature and photon energy combinations at which similar experiments can be performed. Finally, the role of the polarization of the incoming light is evidenced. Original dichroic effects are measured and compared to what are, to the best of our knowledge, the first high energy calculations of angle-resolved photoemission spectra that show this effect.

II. EXPERIMENTAL DETAILS

The experiments have been carried out at the ID08 soft x-ray beamline at the European Synchrotron Radiation Facility in Grenoble, France, where an APPLE II undulator provides a vertically, horizontally, circularly right and left polarized photon beam. The degree of polarization is $\approx 100\%$ for all four polarizations and at all used energies. However, except for Sec. IV C, where both left and right circularly polarized light are used in order to observe the circular dichroism effect, all measured data as well as calculated spectra discussed in this manuscript have been obtained for right circularly polarized light. The beamline is equipped with a Scienta SES-2002 electron analyzer that is coupled to an ultrahigh vacuum chamber.

The (001) surface of a single crystal sample of Ag has been cleaned *in situ* by argon-ion bombardment and annealed at temperatures ranging between 450 and 550 °C in order to remove any surface damage given by the cleaning procedure. Several cleaning cycles are necessary to obtain an optimal surface. Throughout the measurements the base pressure in the main experimental chamber is kept below 10^{-10} mbar. The cleanliness of the surface is checked by monitoring the C and O 1*s* peaks with core level x-ray photoemission spectroscopy (XPS) and both types of contaminations are absent for the whole length of the data acquisition. Low energy electron diffraction (LEED) is used to verify the good surface order and to specify the orientation of the sample. A continuous flow of liquid He allows for the sample cooling and the heating system consists of a spirally wound filament positioned on the sample holder. The experimental geometry is shown in Fig. 1 together with the first BZ of Ag. The angle, ψ, between the incident light and the surface normal is fixed and equal to 35°. The specially built sample holder allows for polar, Θ, and azimuthal, φ, rotations as well as for the adjustment of the additional β angle. Polar rotations are performed about the axis that is perpendicular to the plane containing the direction of x-ray incidence and the surface normal, whereas azimuthal rotations are about the surface normal and the azimuth angle, φ, is measured with respect to the [100] crystallographic direction. The electron emission, defined by the angle ϑ measured with respect to the [001] direction, takes place in a plane that is perpendicular to the one defined by the incoming radiation and the surface normal. It follows that, in contrast to other investigations,[8] and because of the particular geometry chosen in this study, no photon momentum transfer occurs along the electron analyzer's slits. For example, referring to Fig. 1, when $\varphi=0°$, the photon momentum has no component along the [100] direction. However, the effect of the photon momentum along the [010] direction is to "kick" the photoelectron away from the desired high symmetry direction. This effect will be further discussed in Sec. III A for the particular case of $\varphi=45°$. Finally, in order to take into account the photon momentum transferred along the direction that is perpendicular to the sample's surface, the free-electron-like final-state approximation is modified by simply adding a factor $q\cos\psi$ to the

expression that is generally used in the low energy case. If the inner potential is chosen as $V_o=10.5$ eV with respect to the vacuum level,[17] the calculated values of $h\nu$ that identify the location of the high symmetry points along the [001] direction accurately correspond to the experimentally determined values. In particular, the Γ point along this direction has been experimentally determined by measuring spectra (not shown here) as a function of the photon energy, with $h\nu$ varying from 415 to 698 eV. This point is reached for $h\nu=552$ eV.

III. THEORETICAL BACKGROUND AND ONE-STEP MODEL CALCULATIONS

A rigorous description of a photoemission process requires a quantum-mechanical treatment of the complete event during which an electron is removed from an occupied state within a solid and arrives at the detector. Theoretical approaches of this kind treat the photoemission process as a one-step event in which photon absorption, electron removal, and electron detection are considered simultaneously.[33–38]

Within a relativistic description, the determination of the photoemission current starts by solving the Dirac equation. This in turn can be obtained from the relativistic generalization of density functional theory introduced by Rajagopal and Callaway[39] and Ramana and Rajagopal.[40] It can be solved using the phase-functional ansatz of Calogero[41] generalized to the relativistic case.[42–45] From this solution it is easy to define the atomic scattering matrix, t, for a single atom potential together with the wave functions for the initial and for the final state. The atomic scattering matrix, together with the crystal geometry, determines the scattering matrix, M, for a single layer. By means of layer-doubling techniques the so called bulk-reflection matrix can be calculated, which gives the scattering properties of a semi-infinite stack of layers. Finally, applying the spin-polarized low-energy electron diffraction (SPLEED) theory[46–54] one is able to derive the final state and the initial state for the semi-infinite crystal.

According to Pendry[35] the photocurrent consists of four different contributions. The atomic contribution is built up by a product between the matrix $\mathcal{Z}^1$ and the multiple scattering coefficients $A_{jn\kappa\mu}$ of the final state. Herein n denotes the nth cell of the jth layer and κ and μ are the conventional relativistic quantum numbers. For an explicit calculation $\mathcal{Z}^1$ must be separated into angular matrix elements and radial double matrix elements. A detailed description of the matrix $\mathcal{Z}^1$ and of the multiple scattering coefficients $A_{jn\kappa\mu}$ is given in Ref. 38. The intra(inter)layer contributions to the photocurrent describe the multiple scattering corrections of the initial state within and between the layers of the single crystal. They can be written in a similar way to the atomic contribution, the main difference being that the radial part of the intra(inter)layer contributions consists of radial single matrix elements instead of radial double integrals. For a detailed description of these matrix elements and of the corresponding multiple scattering coefficients C^B and C^G the reader again is referred to Ref. 38.

The last contribution takes into account the surface of the semi-infinite crystal.[38] However, for x-ray photoemission calculations the surface contribution can be neglected due to the increased escape depth of the photoelectrons. Added to this, the multiple scattering for the final-state wave field may be neglected simply by setting the Kambe matrix X to zero. This is equivalent to the so-called single-scatterer approximation for the final state. Lifetime effects in the final and initial states have been included in our analysis in a phenomenological way using a parametrized complex inner potential $V_o(E)=V_{or}(E)+iV_{oi}(E)$. Herein the real part serves as a reference energy inside the crystal with respect to the vacuum level. For the final and initial states, constant imaginary parts, $iV_{oi}(E_f)=4.5$ eV and $iV_{oi}(E_i)=0.08$ eV, respectively, have been chosen. The bulk potential used in the photoemission calculations results from a fully relativistic SPR-KKR calculation.[55]

A. q_{par} effect

As already mentioned above, due to the relatively high incoming energies the role played by the photon momentum is no longer negligible, the importance of such an effect depending on the chosen experimental geometry. In particular, referring to Fig. 1, for $\varphi=45°$ the photon momentum has no component along the [110] crystallographic direction. However, the effect of the photon momentum along the $[\bar{1}10]$ direction is to kick the photoelectron in a direction that is perpendicular to the probed high symmetry direction. This effect is experimentally corrected for by rotating the crystal surface by a small amount, $\Theta=0.7°$, with respect to the entrance plane of the electron analyzer, thereby minimizing the effect of the photon momentum transfer along the $[\bar{1}10]$ direction. However, one has to pay the price that the high symmetry plane, in this case the ΓXUL plane, is no longer the plane from which the emission takes place. A careful theoretical analysis reveals that an angle $\Theta=0.7°$ corresponds, for photon energies belonging to the 500–600 eV range and in the local reference frame used for the calculations (i.e., the coordinate system defined with respect to the surface normal), to an effective variation of the angle φ of $\pm 7°$, i.e., $\varphi^*=\varphi\pm 7°$ for the given range of the emission angle θ. Fortunately, the largest deviation appears for nearly normal emission and for higher emission angles it approaches zero. Therefore, the absolute deviation from the high symmetry plane is small and the experiment mainly represents emission from the ΓLUX plane with the added advantage of a minimized q_{par} effect. Figure 2 shows the effect of both the correction angle, Θ, and the photon momentum, q_{par}. In panel A the intensity distribution has been calculated for $\Theta=q_{par}=0$, whereas in panels B and C nonzero values for q_{par} and Θ, respectively, have been used. It is observable that in both panels B and C the band dispersion is more pronounced than in panel A, where the bands appear more flat. This effect, together with an additional asymmetric intensity distribution around Γ, is caused by the small deviation from the desired high symmetry plane mentioned above. Panel D represents the experimental situation with $\Theta=0.7°$ and a nonzero q_{par} value. Observable is the similarity between panels A and D. Therefore, we can conclude that the experimental procedure works successfully and we discuss

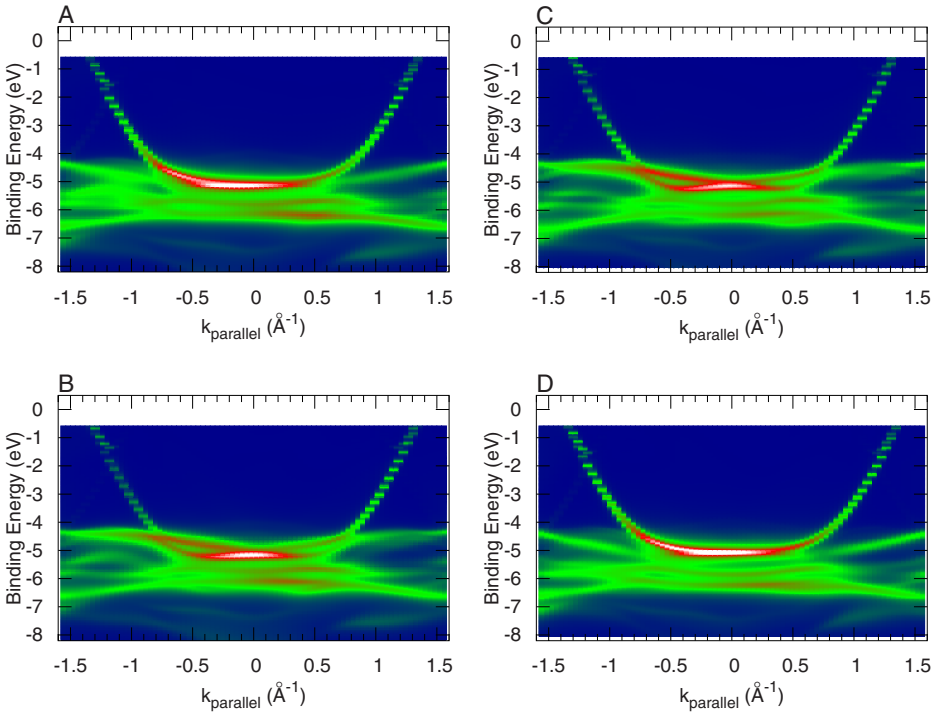

FIG. 2. (Color online) Theoretical photoemission intensity for the Γ-*K* high symmetry direction (Σ) calculated for $h\nu$=552 eV, φ =45°. To allow for a one-to-one comparison between the experimental and the theoretical data, all the theoretical data have been shifted by 1.2 eV. Panel A: intensity distribution calculated for q_{par}=0 and Θ=0°. Panel B: intensity distribution calculated for a nonzero q_{par} vector and Θ=0°. Panel C: intensity distribution calculated for q_{par}=0 and Θ=0.7°. Panel D: intensity distribution calculated for a nonzero value of q_{par} and Θ=0.7°. This corresponds to the experimental geometry setup.

both the experimental and the theoretical data presented in the following using high symmetry notations or the corresponding φ angle.

B. Effect of phonon disorder

The observation of strong direct transition effects in the low and intermediate energy range, and the full BZ averaging that takes place for $h\nu \approx 10^3$ eV, was first explained by Shevchik.[56–58] It appeared that thermal disorder destroys the **k** conservation in a photoemission process and that this phenomenon becomes extremely important for most materials at room temperature and/or x-ray photoemission incoming energies. In particular, two different contributions give rise to the photoemission spectrum: one originates from the **k**-conserving direct transitions, and the other one from the so-called phonon-assisted nondirect transitions. The weaker selection rule imposed on **k** in the latter contribution allows transitions from different regions of the BZ giving rise to density-of-states-like spectra. In the absence of correlations amongst the atoms within the solid, the relative importance of these two contributions is determined by the Debye-Waller factor, $W(T)$ as follows:

$$W(T) = \exp[-G^2 U_0^2(T)], \tag{1}$$

where $U_0^2(T) = T(3h^2/4\pi^2 M_a k_B \theta_D^2)$ is the mean square displacement of the atoms, M_a is the atomic mass, k_B is Boltzmann's constant, and θ_D is the Debye temperature of the investigated system. In addition, Eq. (1) also implies a photon energy dependence given by the change in the reciprocal lattice vector, $\mathbf{G}=\mathbf{K}-(\mathbf{k}+\mathbf{q})$, associated with changing the incoming energy, where **K** is the final-state wave vector. It follows that the nondirect transitions become more significant at high temperatures and/or at high excitation energies. For room temperature photoemission studies direct transition processes should dominate in most metals at ultraviolet photoemission energies, whereas, due to the large value of *G*, the phonon-assisted processes are expected to dominate in the x-ray photoemission regime.

The temperature dependence of the valence band spectra expected as a result of such phonon-induced transitions was experimentally observed in a low energy angle-resolved photoemission experiment performed on Cu.[59] For high incoming photon energies, the temperature dependence of the photoemission spectra suggested in Refs. 56–58 was first observed for tungsten, W.[60,61] In particular, the direct transition component of the photoemitted intensity was found to be consistent with a simple direct transition model based on constant matrix elements and a free-electron-like final state, in agreement with Refs. 62 and 63. On the other hand, the nondirect transition component appeared to be similar to the density of states weighted by the appropriate matrix elements. In more recent investigations[14,15,64] temperature and photon energy dependent angle-resolved photoemission spectra from Al have been analyzed with a model that allows us to calculate the contributions to the photoemitted intensity for transitions in which *m* phonons have been excited or absorbed, with $m=0,1,2,\ldots$. The lattice vibrations are treated within the Debye model and larger vibrational amplitudes at the surface are taken into account. The results clearly show a decay of the direct transition peak with increasing temperature and photon energy that can be qualitatively understood in terms of Shevchik's model. Nevertheless, it is shown that the direct transition peaks also contain contributions from electrons that have been scattered by one or more phonons. Finally, a photon energy dependent investigation of the Fermi surface of Cu performed at room temperature and with $h\nu$ varying between approximately 95 and 260 eV shows that phonon broadening effects are already

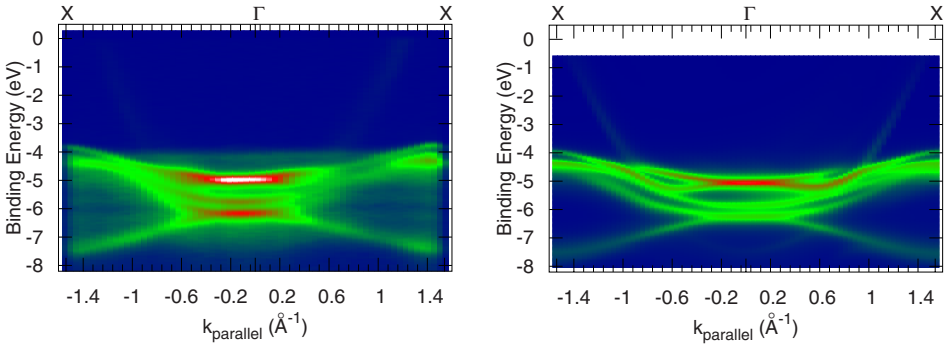

FIG. 3. (Color online) Γ-X high symmetry direction (Δ) probed with $h\nu$=552 eV, φ=0°, and T=20 K. The Fermi level is found at E_F=0 eV. Left: experimental data. Right: theoretical results.

visible in this energy range, although only for the highest investigated photon energies.[65]

IV. EXPERIMENTAL RESULTS AND DISCUSSION

A. Low temperature measurements

Measurements have been taken at T=20 K for two values of the incoming photon energy, $h\nu$=552 eV and $h\nu$ =698 eV, that correspond to the Γ and the X symmetry points along the direction that is perpendicular to the sample's surface. The four data sets are measured with right circularly polarized light. For each measurement the data are normalized both to the current measured at the sample and the acquisition time. The results obtained with $h\nu$=552 eV are shown in the left panels of Figs. 3 and 4, for φ=0° and φ=45°, respectively. For φ=0°, the parallel component of the initial-state wave vector, k_{par}, varies along the Δ direction, whereas for φ=45° the Σ direction is probed. The BZ boundaries along these two directions are found at k_{par} $\approx$1.54 Å^{-1} and $k_{\mathrm{par}}\approx$1.63 Å^{-1}, respectively, and a photon beam of energy $h\nu$=552 eV allows us to probe almost the entire BZ along these directions. In a similar way, Figs. 5 and 6 show the results obtained for $h\nu$=698 eV, with φ=0° and φ=45°. In this case, k_{par} varies along the Z and S high symmetry directions, respectively. Here, the BZ boundaries are found at $k_{\mathrm{par}}\approx$0.73 Å^{-1} and $k_{\mathrm{par}}\approx$0.51 Å^{-1} and with an incoming energy of $h\nu$=698 eV the BZ boundary for both azimuthal orientations is not only reached but crossed. Along the S direction k_{par} varies from X to U=K, and then toward the Γ point belonging to the next BZ. This is observed in Fig. 6, where the s-p band is seen crossing the Fermi level at $k_{\mathrm{par}}\approx\pm$0.9 Å^{-1}. This band is also observed in Fig. 4 where, for a different value of $h\nu$, the energy dispersion from Γ to K is shown. Along the Z direction, k_{par} moves from X to W and back to X again; hence, the obvious periodicity that appears in Fig. 5.

The experimental results shown in Figs. 3 and 4 are in good qualitative agreement with the fully relativistic one-step model photoemission calculations (see Sec. III) shown in the right panels of the respective figures. The approximately 1 eV binding energy shift that is observed with respect to the measurements is due to the missing correlation effects not included in the local density approximation to the density functional theory. The experimental data are also in good qualitative agreement with the theoretical band structure discussed in Ref. 22. Along the Δ and Σ high symmetry directions, direct transitions originating from all the allowed initial states are visible close to the BZ center, except for the two deeper lying bands along both directions. In particular, for both investigated orientations the $\Gamma'_{25}\rightarrow\Gamma^+_8+\Gamma^+_7$ spin-orbit splitting is observed at Γ. Table I shows the binding energies of the high symmetry points along the [001] direction, Γ and X, respectively. The experimental values found in literature[25,26,29] are shown to the right of our results that are listed in the first column. The column to the far right lists the theoretical values found in Ref. 22. The agreement between our results and the ones previously determined in Refs. 26 and 29 is good, with a maximum deviation of 0.22 eV for the most tightly bound X^+_6 energy level. The spin-orbit split level with X^+_7 symmetry is not distinguishable at k_{par}=0 Å^{-1} for $h\nu$=698 eV and is barely visible at the BZ boundary along the Δ direction (Fig. 3). Its binding energy along this direction is given in brackets in Table I.

The angle-resolved photoemission data presented so far show evidence of the fact that, for well-defined combinations of $h\nu$ and temperature, direct transitions in the soft x-ray regime can indeed be observed. If compared to the low energy application of the same technique, the combination of a larger **k**-space sampling and a reduced curvature of the in-

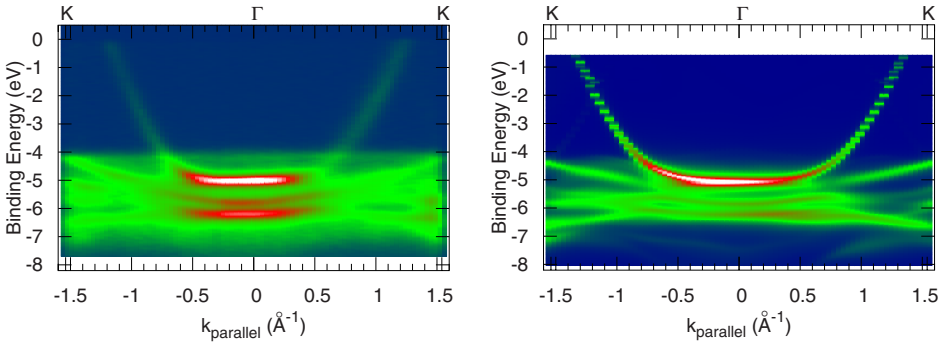

FIG. 4. (Color online) Γ-K high symmetry direction (Σ) probed with $h\nu$=552 eV, φ=45°, and T=20 K. Left: experimental data. Right: theoretical results (copy of panel D in Fig. 2).

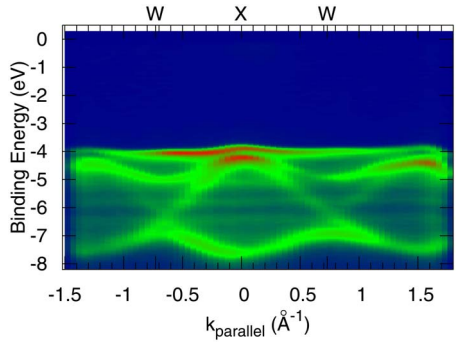

FIG. 5. (Color online) *X*-*W* high symmetry direction (*Z*) probed with $h\nu$=698 eV, φ=0°, and T=20 K.

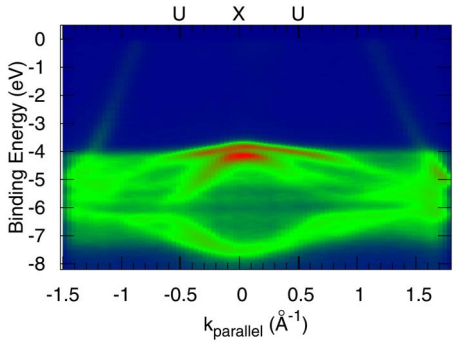

FIG. 6. (Color online) *X*-*U* high symmetry direction (*S*) probed with $h\nu$=698 eV, φ=45°, and T=20 K.

vestigated path, together with the use of a two-dimensional position sensitive detection system, allow measuring the band structure along specific high symmetry directions with a single measurement. This has been done for four different directions, namely, the Δ, Σ, *Z*, and *S* high symmetry directions belonging to the BZ of Ag. The results obtained for T =20 K are in good agreement with our fully relativistic one-step model photoemission calculations.

B. Does band mapping find its limits in the soft x-ray range?

In order to investigate the limits of soft x-ray angle-resolved photoemission spectroscopy both as a function of the measuring temperature and of the incoming photon energy a second set of angle-resolved measurements has been performed. Data have been collected for three different values of the incoming photon energy, $h\nu$=422, 698, and 1040 eV. These values of $h\nu$ correspond to three consecutive *X* points along the [001] direction. The three equivalent high symmetry points are reached with $\mathbf{G}=\frac{4\pi}{a}(\mathbf{0},\mathbf{0},\mathbf{3.5})$, $\mathbf{G}=\frac{4\pi}{a}(\mathbf{0},\mathbf{0},\mathbf{4.5})$, and $\mathbf{G}=\frac{4\pi}{a}(\mathbf{0},\mathbf{0},\mathbf{5.5})$ respectively. The azimuthal angle is kept constant and φ=45°, thereby probing the *S* high symmetry direction. The Debye temperature of Ag is known to be θ_D=215 K and for each value of $h\nu$ measurements have been taken for three different temperatures, T =20, 100, and 215 K. The mean square displacements, $U_0^2(T)$, and Debye-Waller factors, $W(T)$, as obtained from Eq. (1) for each combination of $h\nu$ and T, are listed in Tables II and III, respectively. The data sets shown in the following are normalized to both the current at the sample and the acquisition time and the combined energy resolution of the beamline and the electron analyzer is $\Delta E \approx 90$, 150, and 300 meV for the three investigated values of $h\nu$. Although in principle the chosen values of $h\nu$ probe three equivalent high symmetry points, when the photon energy increases the momentum resolution worsens and the mean free path of the outgoing photoelectrons increases. Hence the spectral features and the intensities of the data sets taken for different values of $h\nu$ at a given temperature cannot be directly compared. All the spectral variations observed with both temperature and photon energy are completely reversible and reproducible.

Figure 7 shows the temperature dependence of the angle-resolved data for $h\nu$=422 eV, $h\nu$=698 eV, and $h\nu$ =1040 eV from left to right. Clearly, the nine measurements give results that are qualitatively in agreement with Shevchik's model.[56–58] Consistently with it, as the temperature and the photon energy are reduced, the phonon-assisted transitions decrease and the measured spectra can be compared with the band structure calculations discussed in Ref. 22. In particular, the results obtained for $h\nu$=422 eV and T =20 K show a strong direct transition behavior. Nevertheless, despite the low values of $h\nu$ and T, three features of constant binding energy are seen crossing the BZ center between approximately 4.7 and 7 eV. These features, which

TABLE I. Binding energies (eV) of the Γ and *X* high symmetry points along the [001] direction. The column to the left lists our experimental results. The value given in parentheses represents the spin-orbit split level visible only at the BZ boundary along the Δ direction.

	This work		Expt.		Theor.[a]
Γ_6^+					7.21
Γ_8^+	6.13	5.92[b]	6.16[c]	6.23[d]	5.82
Γ_7^+	5.73	5.48[b]	5.64[c]	5.80[d]	5.37
Γ_8^+	4.95	4.78[b]	5.00[c]	4.95[d]	4.69
X_6^+	7.58		7.30[c]		7.00
X_7^+					6.82
X_7^+	(4.31)		4.36[c]		4.25
X_6^+	4.20		4.12[c]		4.05
X_7^+	3.87		3.82[c]		3.71

[a]Reference 22.
[b]Reference 25.
[c]Reference 26.
[d]Reference 29.

TABLE II. Mean square displacements, $U_0^2(T)=T(3h^2/4\pi^2 M_a k_B \theta_D^2)$, calculated for three different temperatures. θ_D =215 K.

	T=20 K	T=100 K	T=215 K
$U_0^2(T)$ (Å^2)	0.00058	0.0029	0.0062

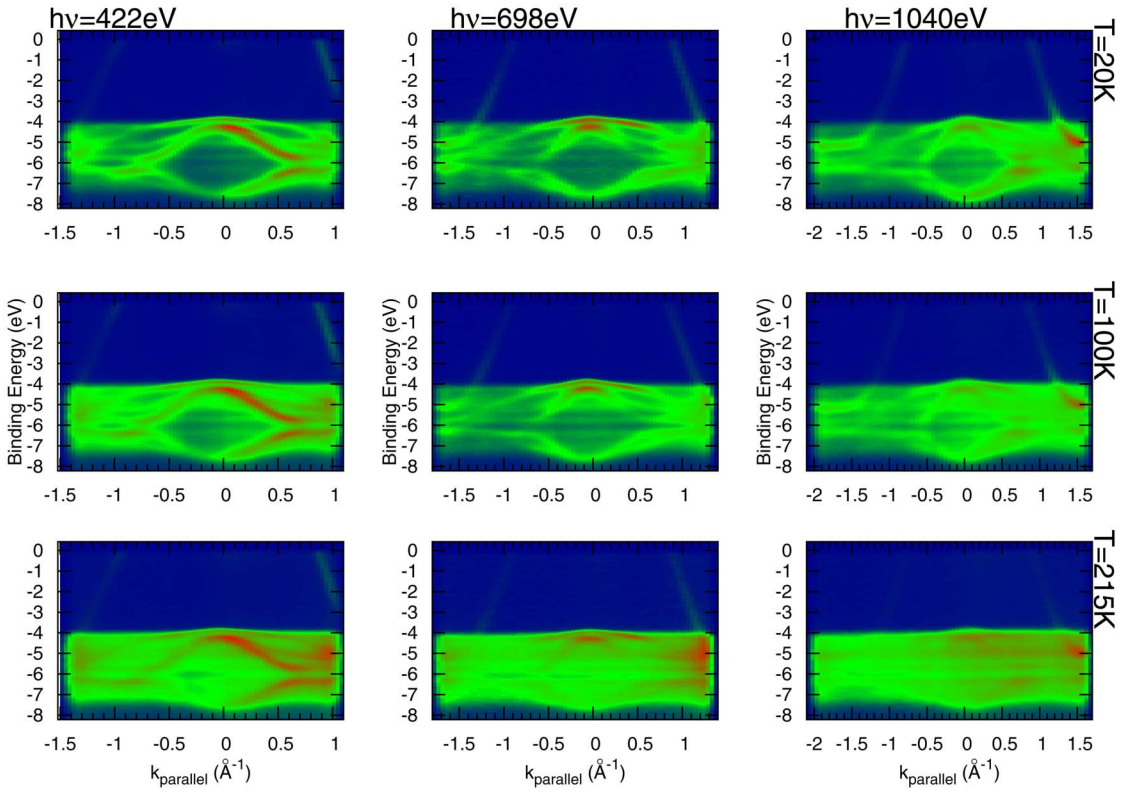

FIG. 7. (Color online) *X-U* high symmetry direction probed for nine different combinations of T and $h\nu$. From left to right: $h\nu$ =422 eV, $h\nu$=698 eV, and $h\nu$=1040 eV. From top to bottom: T=20 K, T=100 K, and T=215 K. E_F=0 eV.

have also been observed in the low energy results presented in Ref. 26, mark the existence of non-**k**-conserving transitions originating from initial states in regions of **k** space that are not directly probed by our experimental geometry.

In Fig. 8, for $h\nu$=422 eV and $h\nu$=1040 eV normal emission (k_{par}=0 Å^{-1}) energy distribution curves are plotted as a function of the temperature. As already mentioned, the structures that appear between approximately 4.7 and 7 eV binding energies in all the spectra are ascribed to the nondirect transitions. It is clearly observed that for a given photon energy as the temperature is raised, the intensity of these features increases, suggesting an increase in the contributions originating from non-**k**-conserving transitions. The same effect can be observed for a given temperature as a function of the photon energy, although the intensities of features measured with different values of $h\nu$ should not be directly compared. For $h\nu$=422 eV three distinct peaks that correspond to direct transitions originating from states having X_7^+ and X_6^+ symmetries are observed at 3.85, 4.18, and 7.48 eV binding energies. These peaks are labeled as *a*, *b*, and *c*, respectively. In a similar way the features arising from the nondirect transitions are labeled as *d*, *e*, and *f*. The spin-orbit split partner of peak *b*, labeled as *g*, is seen as a very weak shoulder that appears on the high energy side of the shallower X_6^+ peak. Despite a broadening of the features and an increase of the phonon-assisted transitions at T=215 K, the direct transition peaks are visible for each temperature. The distinction between peaks *a* and *b* disappears for $h\nu$=1040 eV, where only the X_6^+ peak remains visible and the X_7^+ feature, peak *a*, appears as a weak shoulder.

TABLE III. Debye-Waller factors, $W(T)$, calculated for nine different combinations of T and $h\nu$ according to Eq. (1).

	$h\nu$=422 eV	$h\nu$=698 eV	$h\nu$=1040 eV
T=20 K	0.935	0.895	0.847
T=100 K	0.715	0.574	0.437
T=215 K	0.488	0.305	0.170

Direct transitions originating from the deeper lying X_6^+ level are only visible for T=20 and 100 K but already at T =100 K the broadening of the feature is significant. For T =215 K most of the structure originating from the direct transitions is lost, the intensity between 4.7 and 7 eV increases, and an accurate determination of peak *c* is no longer possible.

In Fig. 9 the ratio of the intensity of peak *c* to the intensity of peak *f* is plotted as a function of the temperature, for the three different values of $h\nu$, for both k_{par}=0 Å^{-1} (left panel) and k_{par}=0.25 Å^{-1} (right panel). However, due to the strong spectral variations induced by the nondirect transitions for $h\nu$=1040 eV and T=215 K, an accurate determination of the ratio is somewhat difficult for this specific combination of $h\nu$ and T. For each value of the photon energy, and for both values of k_{par}, the ratio of the direct to the nondirect transitions decreases with increasing temperature. Added to this, for a given temperature and k_{par}, the contribution of the direct

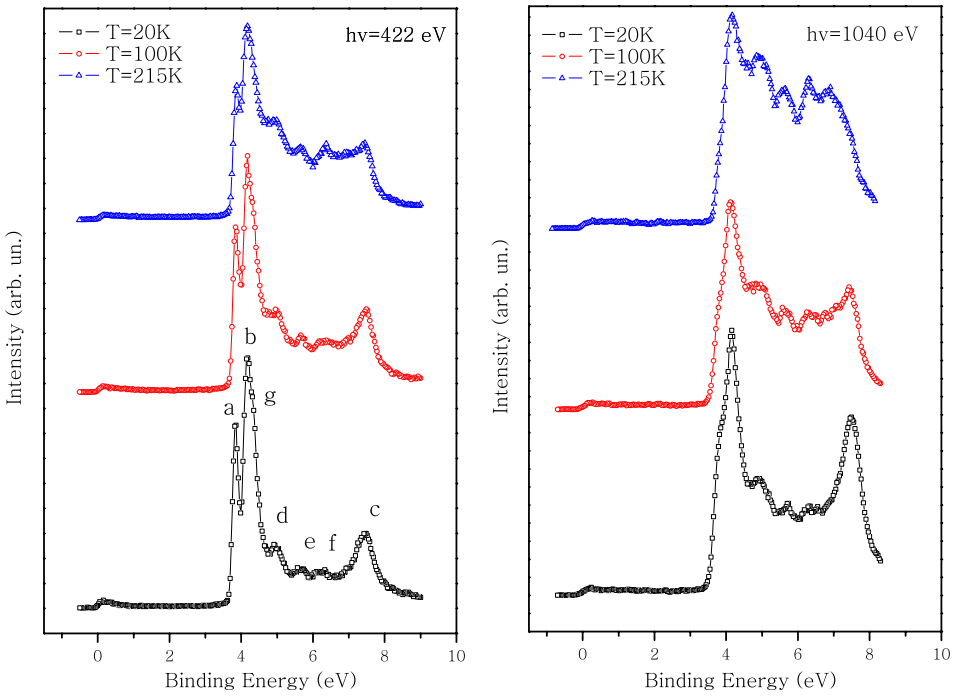

FIG. 8. (Color online) Normal emission (k_{par}=0 Å^{-1}) energy distribution curves as a function of both temperature and photon energy. From left to right the incoming photon energy increases. The temperature increases from bottom to top: □=20 K, ○=100 K, and △=215 K. The direct transition peaks are labeled as *a*, *b*, and *c*; the nondirect contributions as *d*, *e* and *f*. *g* indicates the spin-orbit split partner of peak *b*. The spectra are shifted vertically for clarity and E_F=0 eV.

transitions is strongest at $h\nu$=422 eV and decreases as the photon energy is raised to $h\nu$=1040 eV. It can also be observed that the variation of the plotted ratio with temperature is slightly larger for k_{par}=0.25 Å^{-1}. This is in agreement with the idea that for a given combination of photon energy and temperature, such nondirect transitions are more critical for values of k_{par} for which the band dispersion is more pronounced.[66] Finally, a different way of looking at the same effect is to consider, for a given photon energy, the energy distribution curves as a function of k_{par} for each temperature. This is shown in Fig. 10 for $h\nu$=422 eV (top row) and $h\nu$ =1040 eV (bottom row). What appears is that for $h\nu$ =422 eV the spectra measured with T=20, 100, and 215 K can be directly compared with the band structure calculations discussed in Ref. 22. In particular, at the BZ edge (k_{par} ≈0.5 Å^{-1}) all of the five bands can be observed although the deeper lying one is seen only as a weak shoulder appearing on the high energy side of the spectrum. Nevertheless, at T =215 K a direct comparison with the band structure is more difficult, as the underlying intensity of the nondirect contributions increases. For $h\nu$=1040 eV the situation is different. At T=20 K the direct transition features can still be distinguished but strong modifications of the line shape and of the relative intensities are already visible. On the other hand, the measurements taken with $h\nu$=1040 eV and T=215 K have lost most of their structure and are very similar for each value of k_{par}. If compared to the very recent results published in Ref. 67, where high energy angle-integrated photoemission measurements of the valence band of polycrystalline Ag are successfully compared to the calculated bulk density of

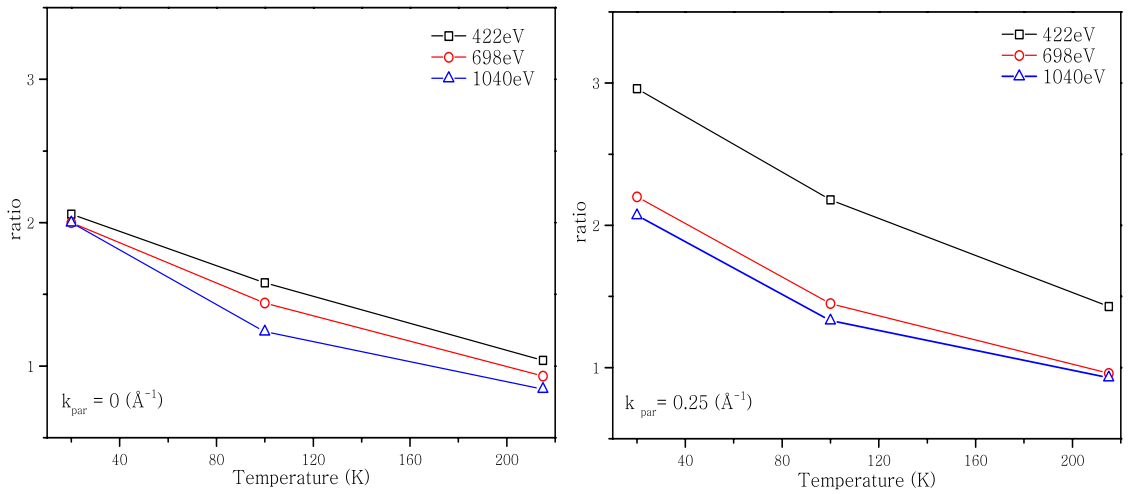

FIG. 9. (Color online) Ratio of the direct transition intensity (peak *c* in Fig. 8) to the nondirect transition intensity (peak *f* in Fig. 8) as a function of T, for $h\nu$=422 eV (□), $h\nu$=698 eV (○), and ν=1040 eV (△). Left: k_{par}=0 Å^{-1}. Right: k_{par}=0.25 Å^{-1}.

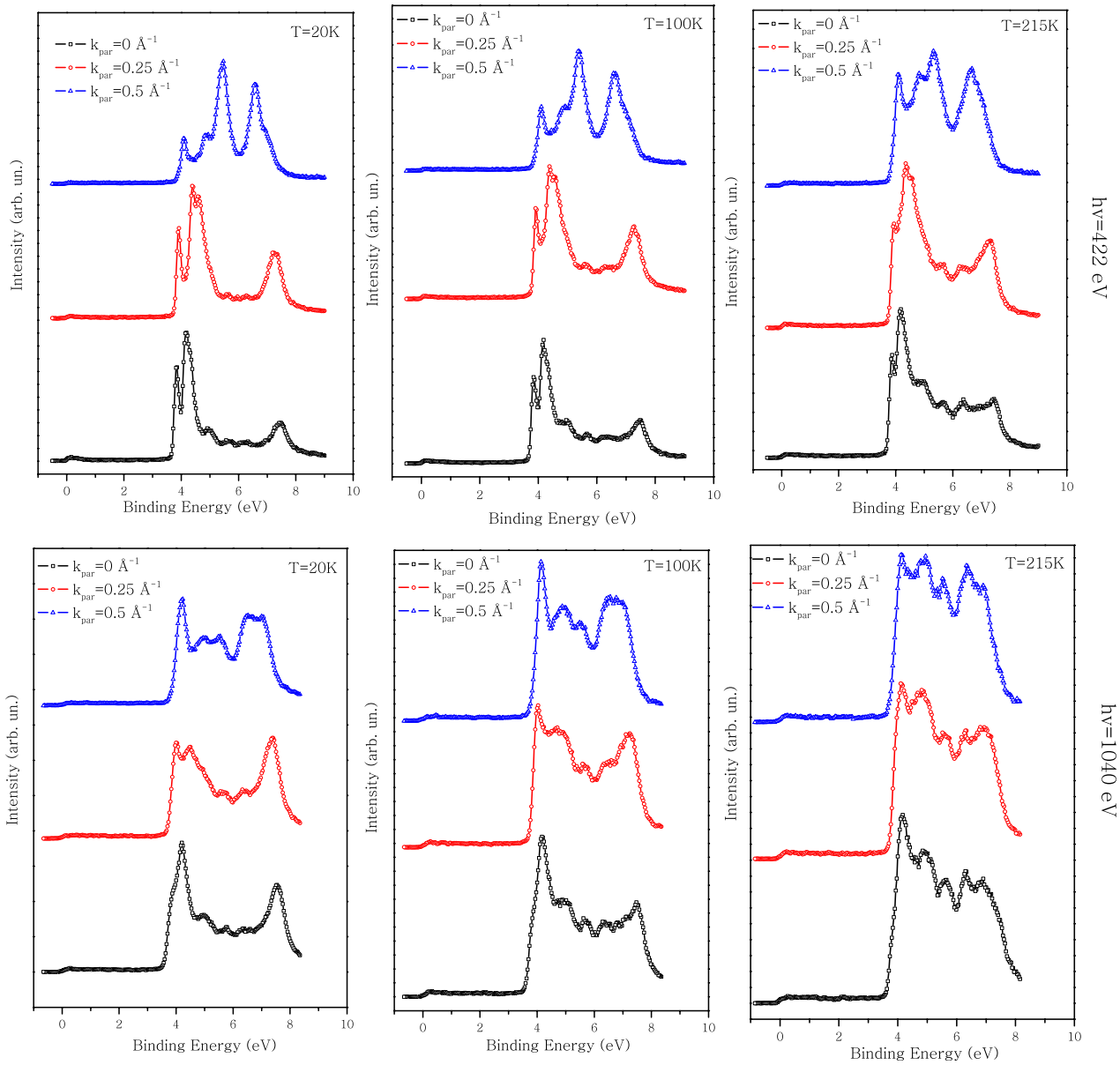

FIG. 10. (Color online) Energy distribution curves plotted as a function of k_{par}, for each temperature and for two different values of $h\nu$. Top row: $h\nu$=422 eV. Bottom row: $h\nu$=1040 eV. The temperature increases from left to right. □=k_{par}=0 Å^{-1}, ○=k_{par}=0.25 Å^{-1}, and △=k_{par}=0.5 Å^{-1}. The data are shifted vertically for clarity and E_F=0 eV.

states, our results show that in the case of Ag (θ_D=215 K), the transition from a bandlike to a density of statelike behavior, called the XPS limit, has already been reached for $h\nu$=1040 eV and T=215 K.

The effects of phonon disorder have been investigated by measuring the same high symmetry direction, S, for three different values of the photon energy and the temperature. For both $h\nu$=422 and 698 eV the direct transition features are visible up to T=100 K and a comparison with the theoretical band structure is possible.[22] At higher temperatures the contribution arising from the phonon-assisted nondirect transitions increases and a general broadening of the spectral line shape is observed. When probing the system with $h\nu$=1040 eV the phonon influence is dominant and even for T=20 K an accurate determination of the direct transition peaks is difficult. Therefore, relatively high energy and momentum resolution soft x-ray angle-resolved photoemission spectroscopy proves to be an accurate technique for sampling the electronic band structure of solids provided the value of the Debye temperature, which must not be too low, is taken into account. Nevertheless, even when the optimal experimental conditions are reached (in the study presented here $h\nu$=422 eV and T=20 K) weak non-**k**-conserving contributions are visible.

C. Circular dichroism in the angular distribution

Circular dichroism in photoemission or, more precisely, circular dichroism in the angular distribution of the photoelectrons (CDAD) from nonchiral species such as diatomic

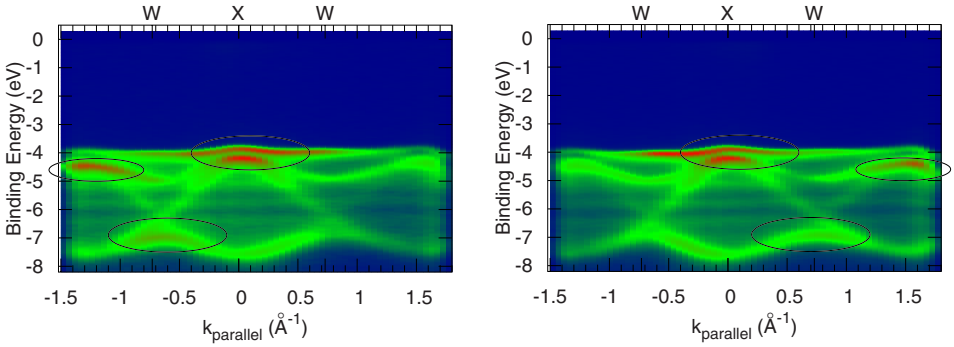

FIG. 11. (Color online) *X*-*W* high symmetry direction (*Z*) probed with circularly left (left panel) and circularly right (right panel) polarized light respectively. $h\nu$=698 eV, φ=0°, and T=20 K. The areas of interest for the CDAD effect are circled in black. E_F=0 eV.

molecules, provided they are spatially oriented, was first predicted in Ref. 68. If compared to common circular dichroism effects, a substantial difference is that CDAD occurs already in the pure electric dipole transition.[69] In the low energy range, circular dichroism in the angular distribution of the photoelectrons has been observed for adsorbed molecules on transition metal surfaces[70,71] and for several surfaces, amongst which graphite (0001), Pd(111), and Si(001).[72,73] As a general rule, circular dichroic effects appear when the system defined by the incoming light and the investigated sample exhibit a definite handedness that gives rise to an asymmetric response to photons of different helicity. In the particular case of angle-resolved photoemission spectroscopy, the crucial handedness of the experimental setup is defined via the noncoplanar spatial arrangement of the incoming photon beam, the momentum of the outgoing electron, and the normal to the sample's surface. This is the case of our experimental geometry shown in Fig. 1. When φ=0°, the operator of circularly polarized light in the reference frame of the crystal surface takes the form of

$$O_{\mathrm{ph}} = \hat{z}\sin 35^\circ + \hat{y}\cos 35^\circ \pm i\hat{x}, \tag{2}$$

where ψ=35° is the angle of incidence of the light with respect to the normal. The incident photon beam will then exhibit a left or right circular polarization depending on the last term in Eq. (2). As a consequence, depending on the photon operator components that intervene for a given transition, the matrix elements may switch sign when changing from one helicity of the light to the other, causing the dichroic effect.

An example can be seen in Fig. 11. The data are taken at φ=0° and $h\nu$=698 eV, with circular left (left panel) and right (right panel) polarized light, respectively. A clear intensity modulation is shown upon switching the polarization of the light. The areas of interest are circled in black in Fig. 11. The distribution of the photoemitted intensity in the negative part of the emission plane in the left panel of Fig. 11 is equivalent to the intensity distribution obtained for positive values of k_{par} in the right panel of the same figure, showing that the dichroic effect is invariant upon application of the operator that changes both the photon helicity and the handedness of the vector arrangement. It is important to mention that the intensity distributions presented in Fig. 11 repeat only approximately with the BZ periodicity. This is due to the experimental correction angle Θ which guarantees a minimized q_{par} effect. However, as explained in Sec. III A, such a correction introduces a slight deviation from the desired high symmetry plane, namely, the *Z* high symmetry direction in this case. Hence, only an approximate repetition of the CDAD features with the periodicity of the zone is observed.

For the experimental geometry shown in Fig. 1, when φ =0°, a reflection of the photoelectron momentum with respect to the normal to the sample's surface is equivalent to a change of photon helicity. Therefore, the dichroic effect can also be observed by comparing the results obtained, for a given polarization, for both positive and negative values of k_{par} belonging to the same emission plane. If compared to the use of linearly polarized light that allows, upon switching from vertical to horizontal, us to determine the symmetry of the initial states for a given experimental geometry, the circular dichroism effect in the angular distribution of the photoelectrons reflects the different partial wave composition of the initial states. Finally, the theoretical method described in Ref. 32 has recently allowed us to calculate this effect. The results are shown in Fig. 12 for the *Z* high symmetry direction, calculated for $h\nu$=698 eV. One has to note here that, for technical reasons, the one-step model photoemission LEED formalism presented in Sec. III until now does not

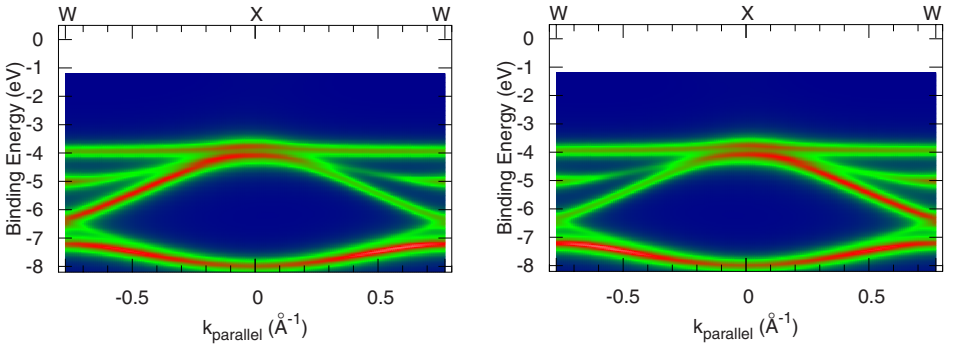

FIG. 12. (Color online) Calculated angle-resolved photoemission spectrum relative to the *X*-*W* high symmetry direction. $h\nu$ =698 eV. Left panel: circularly left polarized light. Right panel: circularly right polarized light. The intensity asymmetry typical of the CDAD effect is reproduced.

allow us to perform photoemission calculations for high symmetry directions which do not cross the Γ point. Nevertheless, given the fact that the dichroic effect is particularly pronounced along the Z direction, we wish to present calculations for this particular direction in **k** space that have been obtained with another fully relativistic multiple scattering code[55] that concentrates explicitly on a quantitative description of the dichroic effect. This formalism works in a three-dimensional bulk mode[32] and as such ignores surface emission and q_{par} effects, which fortunately are of minor importance in this situation.

The approximately 1 eV binding energy shift that is observed with respect to the measurements is due to the fact that, although the code described in Ref. 32 allows for many-body correlation effects, such an implementation has not been used for these theoretical results obtained for Ag, where the correlation effects are small but nevertheless present. A similar but larger discrepancy has recently been observed in Ref. 67.

The overall agreement between the measured and the calculated CDAD effect is quantitative when shifting the bands in energy by about 1 eV. The intensity modulation observed in the experiment is well reproduced and only some small deviations concerning the intensity distributions are observable. This is a typical matrix element effect mostly due to the fact that we neglect in our calculations the influence of q_{par} or, in other words, we move strictly along the Z high symmetry direction in **k** space. On the other hand the calculations demonstrate once again the influence of the q_{par} vector, which forces the intensity distributions to be more asymmetric.

V. CONCLUSIONS

The investigation performed on the (001) surface of Ag addresses several questions regarding the application of angle-resolved photoemission spectroscopy in the soft x-ray energy range. In particular, based on one-step model calculations, we discuss to what extent the photon momentum, q_{par}, influences accurate band mapping. We show that the so-called q_{par} effect is indeed present in the soft x-ray energy range but that a careful choice of the experimental geometry can allow us to control it and thereby minimize it.

Despite the accuracy of the results obtained at low temperature ($T=20$ K) for $h\nu=552$ and 698 eV, the temperature and photon energy dependent study also discussed clearly shows the onset, in the high T and/or in the high photon energy range, of the nondirect transitions caused by the breakdown of the **k**-conservation laws. Our results show that the contribution of the nondirect transitions to the photoemitted intensity is indeed controlled by a delicate balance between $h\nu$ and T. However, precise soft x-ray band mapping is possible if restricted to a rather small range of temperatures and photon energies.

ACKNOWLEDGMENTS

This work was funded by the German BMBF (Bundesministerium für Bildung und Forschung) under Contract No. FKZ 05 KS1WMB/1.

[1] S. Hüfner, J. Phys. Soc. Jpn. **74**, 34 (2003).
[2] F. J. Himpsel, Adv. Phys. **32**, 1 (2005).
[3] T. Kiss *et al.*, Phys. Rev. Lett. **94**, 057001 (2005).
[4] Y. Baer, M. G. Garnier, D. Purdie, P. Segovia, and M. Hengsberger, J. Electron Spectrosc. Relat. Phenom. **114**, 257 (2001).
[5] L. Duó, Surf. Sci. Rep. **32**, 235 (1998).
[6] T. Claesson, M. Mansson, C. Dallera, F. Venturini, C. De Nadaï, N. B. Brookes, and O. Tjernberg, Phys. Rev. Lett. **93**, 136402 (2004).
[7] F. Venturini, J. C. Cezar, C. De Nadaï, P. C. Canfield, and N. B. Brookes, J. Phys.: Condens. Matter **18**, 9221 (2006).
[8] N. Kamakura, Y. Takata, T. Tokushima, Y. Harada, A. Chainani, K. Kobayashi, and S. Shin, Phys. Rev. B **74**, 045127 (2006).
[9] J. J. Yeh and I. Lindau, At. Data Nucl. Data Tables **32**, 1 1985.
[10] S. Suga and S. Sekiyama, J. Electron Spectrosc. Relat. Phenom. **124**, 81 (2002).
[11] S. Suga *et al.*, Phys. Rev. B **70**, 155106 (2004).
[12] A. Sekiyama, Ph. Hofmann, Ch. Sondergaard, S. Agergaard, S. V. Hoffmann, J. E. Gayone, G. Zampieri, S. Lizzit, and A. Baraldi, Phys. Rev. B **70**, 060506(R) (2004).
[13] A. Sekiyama and S. Suga, J. Electron Spectrosc. Relat. Phenom. **137-40**, 681 (2004).
[14] C. Sondergaard, P. Hofmann, C. Schultz, S. M. Moreno, J. E. Gayone, M. A. Vicente Alvarez, G. Zampieri, S. Lizzit, and A. Baraldi, Phys. Rev. B **63**, 233102 (2001).
[15] Ph. Hofmann, Ch. Sondergaard, S. Agergaard, S. V. Hoffmann, J. E. Gayone, G. Zampieri, S. Lizzit, and A. Baraldi, Phys. Rev. B **66**, 245422 (2002).
[16] E. C. Snow, Phys. Rev. **172**, 708 (1968).
[17] N. E. Christensen, Phys. Status Solidi B **54**, 551 (1972).
[18] N. V. Smith, Phys. Rev. B **9**, 1365 (1974).
[19] O. Jepsen, D. Glötzel, and A. R. Mackintosh, Phys. Rev. B **23**, 2684 (1981).
[20] A. H. MacDonald, J. M. Daams, S. H. Vosko, and D. D. Koelling, Phys. Rev. B **25**, 713 (1982).
[21] R. L. Benbow and N. V. Smith, Phys. Rev. B **27**, 3144 (1983).
[22] H. Eckardt, L. Fritsche, and J. Noffke, J. Phys. F: Met. Phys. **14**, 97 (1984).
[23] H. Becker, E. Dietz, U. Gerhardt, and H. Angermüller, Phys. Rev. B **12**, 2084 (1975).
[24] G. V. Hansson and S. A. Flodström, Phys. Rev. B **17**, 473 (1978).
[25] P. S. Wehner, R. S. Williams, S. D. Kevan, D. Denley, and D. A. Shirley, Phys. Rev. B **19**, 6164 (1979).
[26] R. Courths, V. Bachelier, and S. Hüfner, Solid State Commun. **38**, 887 (1981).
[27] H. A. Padmore, C. Norris, G. C. Smith, C. G. Larsson, and D. Norman, J. Phys. C **15**, L155 (1982).
[28] R. Courths, H. Wern, U. Hau, B. Cord, V. Bachelier, and S. Hüfner, J. Phys. F: Met. Phys. **14**, 1559 (1984).
[29] J. G. Nelson, S. Kim, W. J. Gignac, R. S. Williams, J. G. Tobin, S.

W. Robey, and D. A. Shirley, Phys. Rev. B **32**, 3465 (1985).
[30] S. C. Wu, C. K. C. Lok, J. Sokolov, J. Quinn, Y. S. Li, D. Tian, and F. Jona, J. Phys.: Condens. Matter **1**, 4795 (1998).
[31] U. König, P. Weinberger, J. Redinger, H. Erschbaumer, and A. J. Freeman, Phys. Rev. B **39**, 7492 (1989).
[32] J. Minár, S. Chadov, H. Ebert, and L. Chioncel, Nucl. Instrum. Methods Phys. Res. A **547**, 151 (2005).
[33] G. D. Mahan, Phys. Rev. B **2**, 4334 (1970).
[34] P. J. Feibelman and D. E. Eastman, Phys. Rev. B **10**, 4932 (1974).
[35] J. B. Pendry, Surf. Sci. **57**, 679 (1976).
[36] J. F. L. Hopkinson, J. B. Pendry, and D. J. Titterington, Comput. Phys. Commun. **19**, 69 (1980).
[37] B. Ginatempo, P. J. Durham, and B. I. Gyorffy, J. Phys. C **1**, 6483 (1983); S. V. Halilov, E. Tamura, H. Gollisch, D. Meinert, and R. Feder, J. Phys.: Condens. Matter **5**, 3859 (1993); J. Henk, S. V. Halilov, T. Scheunemann, and R. Feder, Phys. Rev. B **50**, 8130 (1994); M. Fluchtmann, M. Graß, J. Braun, and G. Borstel, *ibid.* **52**, 9564 (1995).
[38] J. Braun, Rep. Prog. Phys. **59**, 1267 (1996).
[39] A. K. Rajagopal and J. Callaway, Phys. Rev. B **7**, 1912 (1973).
[40] M. V. Ramana and A. K. Rajagopal, Adv. Chem. Phys. **54**, 231 (1983).
[41] F. Calogero, *Variable Phase Approach to Potential Scattering* (Academic, New York, 1967).
[42] H. Ebert and B. L. Gyorffy, J. Phys. F: Met. Phys. **18**, 451 (1988).
[43] A. Gonis, *Green Functions for Ordered and Disordered Systems*, Studies in Mathematical Physics Vol. 4 (North-Holland, Amsterdam, 1992).
[44] X. Wang, X. G. Zhang, W. H. Butler, G. M. Stocks, and B. N. Harmon, Phys. Rev. B **46**, 9352 (1992).
[45] S. C. Lovatt, B. L. Gyorffy, and G. Y. Guo, J. Phys.: Condens. Matter **5**, 8005 (1993).
[46] W. Kohn and N. Rostoker, Phys. Rev. **94**, 1111 (1954).
[47] A. R. Williams and J. van W. Morgan, J. Phys. C **7**, 37 (1974).
[48] R. Feder, J. Phys. C **14**, 2049 (1981).
[49] R. G. Brown and M. Ciftan, Phys. Rev. B **27**, 4564 (1983).
[50] A. Gonis, X. G. Zhang, and D. M. Nicholson, Phys. Rev. B **40**, 947 (1989).
[51] X. G. Zhang, A. Gonis, and J. M. MacLaren, Phys. Rev. B **40**, 3694 (1989).
[52] W. H. Butler and R. K. Nesbet, Phys. Rev. B **42**, 1518 (1990).
[53] R. K. Nesbet, Phys. Rev. B **41**, 4948 (1990).
[54] W. H. Butler, A. Gonis, and X. G. Zhang, Phys. Rev. B **45**, 11527 (1992).
[55] H. Ebert, The Munich SPR-KKR package, version 2.1.1; http://olymp.cup.uni-muenchen.de/ak/ebert/SPRKKR
[56] N. J. Shevchik, Phys. Rev. B **16**, 3428 (1977).
[57] N. J. Shevchik, J. Phys. C **10**, L555 (1977).
[58] N. J. Shevchik, Phys. Rev. B **20**, 3020 (1979).
[59] R. S. Williams, P. S. Wehner, J. Stöhr, and D. A. Shirley, Phys. Rev. Lett. **39**, 302 (1977).
[60] Z. Hussain, C. S. Fadley, S. Kono, and L. F. Wagner, Phys. Rev. B **22**, 3750 (1980).
[61] Z. Hussain, S. Kono, R. E. Connelly, and C. S. Fadley, Phys. Rev. Lett. **44**, 895 (1980).
[62] R. J. Baird, L. F. Wagner, and C. S. Fadley, Phys. Rev. Lett. **37**, 111 (1976).
[63] L. F. Wagner, Z. Hussain, C. S. Fadley, and R. J. Baird, Solid State Commun. **21**, 453 (1977).
[64] M. A. Vicente Alvarez, H. Ascolani, and G. Zampieri, Phys. Rev. B **54**, 14703 (1996).
[65] M. B. Nielsen, Z. Li, S. Lizzit, A. Goldoni, and Ph. Hofmann, J. Phys.: Condens. Matter **15**, 6919 (2003).
[66] R. C. White, C. S. Fadley, M. Sagurton, P. Roubin, D. Chandesris, J. Lecante, C. Guillot, and Z. Hussain, Phys. Rev. B **35**, 1147 (1987).
[67] G. Panaccione *et al.*, J. Phys.: Condens. Matter **17**, 2671 (2005).
[68] B. Ritchie, Phys. Rev. A **12**, 567 (1975).
[69] N. A. Cherepkov, Chem. Phys. Lett. **87**, 344 (1982).
[70] G. Schönhense, Phys. Scr., T **T31**, 255 (1990).
[71] G. H. Fecher, A. Oelsner, C. Ostertag, and G. Schönhense, J. Electron Spectrosc. Relat. Phenom. **52**, 613 (1990).
[72] G. Schönhense, C. Westphal, J. Bansmann, M. Getzlaff, J. Noffke, and L. Fritsche, Surf. Sci. **251-252**, 131 (1991).
[73] K. Nakatsuji, H. Daimon, T. Furuhata, H. Takagi, M. Fujikawa, S. Suga, T. Miyahara, A. Yagishita, C. H. Solterbeck, and W. Schattke, J. Electron Spectrosc. Relat. Phenom. **88-91**, 213 (1998).